High-Resolution Determination of Soft Tissue Deformations Using MRI and First-Order Texture Correlation

Christopher L. Gilchrist, Jessie Q. Xia, Lori A. Setton, and Edward W. Hsu*, *Member, IEEE*

***Abstract*—Mechanical factors such as deformation and strain are thought to play important roles in the maintenance, repair, and degeneration of soft tissues. Determination of soft tissue static deformation has traditionally only been possible at a tissue's surface, utilizing external markers or instrumentation. Texture correlation is a displacement field measurement technique which relies on unique image patterns within a pair of digital images to track displacement. The technique has recently been applied to MR images, indicating the possibility of high-resolution displacement and strain field determination within the mid-substance of soft tissues. However, the utility of MR texture correlation analysis may vary amongst tissue types depending on their underlying structure, composition, and contrast mechanism, which give rise to variations in texture with MRI. In this study, we investigate the utility of a texture correlation algorithm with first-order displacement mapping terms for use with MR images, and suggest a novel index of image "roughness" as a way to decrease errors associated with the use of texture correlation for intra-tissue strain measurement with MRI. We find that a first-order algorithm can significantly reduce strain measurement error, and that an image "roughness" index correlates with displacement measurement error for a variety of imaging conditions and tissue types.**

***Index Terms*—Biological soft tissues, biomedical magnetic resonance imaging, image texture analysis, strain measurement, texture correlation.**

I. Introduction

THE primary function of musculoskeletal soft tissues is to support and transfer loads within the body. In response to these mechanical loads, physical factors within the tissue such as matrix deformation, hydrostatic pressure and interstitial fluid flow are known to vary [1], [2]. Cells located within these tissues play a critical role in the tissue's maintenance and repair, and these functions are thought to be regulated in part by the mechanical stimuli experienced by the cell [1]–[3]. Additionally, in many pathological situations the mechanical properties of the tissue and the resulting mechanical stimuli experienced by the cell are known to be altered [4]–[6]. The particular set of mechanical stimuli that cells within a given tissue experience and respond to are not well understood, in part due to the lack of knowledge of the deformation state within these tissues in physiologic situations. Traditionally, information about soft tissue deformation has only been available at a tissue's surface via external markers or instrumentation. Thus the development of a noninvasive mid-substance deformation measurement technique is of great potential utility.

Magnetic resonance (MR) imaging offers the potential to obtain two-dimensional (2-D) and three-dimensional (3-D) images within tissue volumes. Numerous acquisition and image analysis techniques have been applied to MR images toward the goal of tracking displacement fields within tissues (e.g., myocardium, breast). These techniques, which include MR elastography [7], tagging [8], phase contrast [9], and DENSE [10], require the tissue of interest to be in periodic motion because the "markers" used are transient in nature. However, the 2-D and 3-D strain fields generated by static joint loads are important in the study of musculoskeletal soft tissues such as cartilage, ligament, and tendon, and cannot be determined via these methods. Heberhold and co-workers have been successful in tracking changes in cartilage layer thickness under static load, or nominal tissue strains, by using MRI to reconstruct articular cartilage layer geometry [11]. This approach does not readily lend itself to estimating the complex heterogeneous strain fields that may exist in tissues under physiological loads. Alternatively, finite element warping has recently been used to track displacements in successive MR images of statically deformed tissues [12], [13], yet requires *a priori* assumptions about material properties and constitutive behaviors that may be unknown or vary with tissue regions or pathological state.

Digital image correlation (DIC) has been shown to be a promising noncontacting, nondestructive technique for measuring 2-D and 3-D static displacement fields via a variety of different imaging modalities, including optical imaging and scanning-tunneling microscopy [14], [15]. Bay [16] applied this method to digitized contact radiographs of a biologic material (trabecular bone), calculating displacement and strain fields by utilizing the inherent heterogeneous patterns of the material's image, or "texture," to track displacement between a reference and deformed image. This DIC method, termed texture correlation, is a pattern matching technique based on the assumption that a pixel within an image can be identified by a unique intensity pattern of pixels surrounding it (called the pixel subset), and that the intensity pattern of the subset

Manuscript received November 29, 2003; revised January 9, 2004. This work was supported by the National Institutes of Health (NIH) under Grant AR47442, Grant AR46407, Grant P41 05959 and Grant T32 GM08555-09). The Associate Editor responsible for coordinating the review of this paper and recommending its publication was A. Manduca. *Asterisk indicates corresponding author.*

C. L. Gilchrist and J. Q. Xia are with the Department of Biomedical Engineering, Duke University, Durham, NC 27708 USA.

L. A. Setton is with the Departments of Biomedical Engineering and Orthopaedic Surgery, Duke University, Durham, NC 27708 USA.

*E. W. Hsu is with the Department of Biomedical Engineering, Duke University, Durham, NC 27708 USA (e-mail: edward.hsu@duke.edu).

Digital Object Identifier 10.1109/TMI.2004.825616

undergoes a displacement that corresponds to the in-plane displacement of the corresponding material element (or volume). Bay [16] and others [17] have found this technique to give excellent results for measuring strain in bone (strain levels of approximately 1%–4%), as compared with tracking markers placed on the surface of a specimen. Recently, the feasibility of using texture correlation to calculate tissue strain fields from 2-D MR images of a soft tissue (tendon) has been examined [18]. The results of this study indicate that MR images may be reproducible enough to track pixel displacements between successive images (depending on image noise level), and that MR images of tendon exhibit suitable texture for tracking pixel displacement. Although these results are promising for the potential to apply texture correlation to MR images for soft tissue strain determination, the accuracy of the MRI texture correlation and its applicability to other tissue types have not yet been fully investigated.

There are several challenges to understanding and improving MR texture correlation accuracy with soft tissues. Displacement and strain measurement accuracy in previous texture correlation studies [16], [18] may have been limited by use of a zeroth-order DIC algorithm, which assumes square pixel subsets remain square in consecutive images. Introducing higher-order subset mapping terms can reduce displacement measurement error [15], [19], [20] and may be particularly important for studying the complex, highly heterogeneous displacement fields that exist in many biological tissues. However, it is unclear whether an algorithm utilizing higher-order mapping terms, which relies on accurate calculations of spline interpolations and the derivatives of the spline functions to efficiently determine the best mapping, will provide accurate results when applied to high-resolution MR images that may contain significant noise.

Additionally, the range of tissue types and MR image characteristics that provide low displacement measurement error with MR texture correlation have not been characterized. Accurate displacement measurement using texture correlation requires that each pixel to be tracked have an adequate amount of texture compared to the image noise level; that is, the intensity pattern of the pixel's subset mask must uniquely identify it in subsequent images and be distinct from the image noise. Since the texture of an MR tissue image is directly dependent upon the structure and composition of the tissue, the amount of texture for any given pixel's subset mask may vary significantly depending on tissue type and location within the tissue. In this study, we propose that a quantitative measure of texture, for pixels within the reference image, would provide the texture correlation user with an estimate of expected displacement error, thus permitting *a priori* selection of optimal pixels for tracking displacement while minimizing error.

The objectives of this study were to implement an advanced texture correlation algorithm for high-resolution tissue displacement tracking and investigate its utility for application to MR images. The first objective was to investigate if the use of first-order displacement mapping terms in the texture correlation algorithm can reduce displacement tracking error and strain measurement error for MR images of representative biological tissues, as compared to the algorithm with zeroth-order mapping terms. Performance of the two algorithms was compared for a range of parameters using simulated displacement data, which allowed for systematic evaluation under precisely controlled conditions. A preliminary demonstration of high-resolution strain field measurement was then carried out using the first-order algorithm and data from a real MR experiment. The second objective was to propose and evaluate a novel parameter to estimate texture from reference images of any soft tissue, toward the goal of reducing displacement tracking error through selection of optimal tracking points.

II. Theory

A. Texture Correlation With First- Order Displacement Gradients

We implemented a texture correlation algorithm with first-order displacement mapping terms as presented by Vendroux and Knauss [15]. Briefly, a square subset of pixels centered about a pixel of interest was mapped from the reference (i.e., before-load) image to the deformed (after-load) image. The coordinates of each subset point (x, y) in the reference image were mapped to their counterpart $(\tilde{x}, \tilde{y})$ in the deformed image using

$$\begin{aligned} \tilde{x} &= x + U(x, y) \\ \tilde{y} &= y + V(x, y) \end{aligned} \tag{1}$$

where U and V are the displacement components between images. Letting (x_0, y_0) be the coordinates for the center of the subset (i.e., the pixel of interest), (1) was expanded about (x_0, y_0) using a first-order Taylor expansion to give

$$\begin{aligned} \tilde{x} &= x + U_0 + U_x \Delta x + U_y \Delta y \\ \tilde{y} &= y + V_0 + V_x \Delta x + V_y \Delta y \end{aligned} \tag{2}$$

where $\Delta x = x - x_0$, $\Delta y = y - y_0$. In this equation, U_0 and V_0 are the zeroth-order displacement components, and U_x, U_y, V_x, and V_y are the first-order displacement gradients for (x_0, y_0). Piecewise continuous bicubic spline interpolation was used to calculate gray-scale pixel intensities and ensure continuous second-order gradients at any location within the reference and deformed images.

To account for variations in image intensity between successive images that was not related to tissue deformation (e.g., spatial variation of RF coil sensitivity), a mapping parameter, w [15], [20], was included to represent the intensity offset between images. This term was incorporated in the bicubic interpolation equation for the deformed image as

$$h(\tilde{x}, \tilde{y}) = \sum_{m=0}^{3} \sum_{n=0}^{3} \alpha_{mn} \tilde{x}^m \tilde{y}^n + w \tag{3}$$

where h represents the image intensity value at a point $(\tilde{x}, \tilde{y})$ in the deformed image and α the bicubic spline coefficients. A least-squares correlation coefficient, C, was used to determine the optimum displacement mapping parameters

$$C = \frac{\sum_{S_p \in S} (g(S_p) - h(S_p, \mathbf{P}))^2}{\sum_{S_p \in S} (g^2(S_p))} \tag{4}$$

where S is the subset of pixels (the subset mask) for identifying a particular pixel of interest, S_p is an individual pixel in the ref-

erence image within the subset mask, $\mathbf{P}$ is a vector containing the seven mapping parameters (U_0, V_0, U_x, U_y, V_x, and V_y, w) that map each subset point S_p to the deformed image, and g and h are intensity values within the reference and deformed images, respectively. To efficiently find a minimum value for C, a Newton-Raphson optimization procedure using a numerical approximation for $\nabla^2 C$ was implemented [15]. Initialization of the $\mathbf{P}$ vector for the iterative procedure was accomplished using the integer values of U_0 and V_0 that minimize C within a search region, with displacement derivatives and w set to zero. The first-order texture correlation algorithm was compared with a zeroth-order algorithm [16] which uses only U_0 and V_0 mapping terms from (2) and a cross-correlation coefficient given by Chu *et al.* [19]. For this algorithm, displacement estimates were refined to the subpixel level using discrete bicubic spline interpolation (e.g., nearest 1/16th pixel), and pixel subsets were compared using a line-search algorithm.

III. Methods

A. Magnetic Resonance Imaging

MR images of canine knee menisci ($\mathrm{n} = 2$) and porcine intervertebral discs ($\mathrm{n} = 3$), obtained previously in separate studies, were used to study algorithm accuracy and texture via controlled computer simulations. Both structures are important contributors to load support and flexibility of the diarthrodial joint and spine, respectively. The meniscus is a crescent-shaped fibrocartilaginous tissue that contains circumferentially arranged collagen fiber bundles distributed throughout. A 9.4-T scanner (Oxford Magnet, Oxfordshire, U.K.) was used to acquire 2-D axial images of the meniscal samples using a standard spin-echo sequence (256×256 matrix size, 98 μm in-plane resolution, 120 μm slice thickness, $\mathrm{TR} = 275$ ms, $\mathrm{TE} = 10$ ms, 8 averages). The MR images of the meniscus reveal the patterns of the aligned collagen bundles, as shown in Fig. 1(a).

The intervertebral disc is a composite tissue consisting of a fibrocartilaginous anulus fibrosus region and a centrally-situated, gelatinous nucleus pulposus region. Two-dimensional axial images were obtained of the intervertebral disc with a 7.1-T scanner (Bruker Instruments, Fremont, CA) using a standard spin-echo sequence (256×256 matrix size, 234 μm in-plane resolution, 469 μm slice thickness, $\mathrm{TR} = 250$ ms, $\mathrm{TE} = 7.6$ ms, 2 averages). In axial MR images of the disc [Fig. 1(b)], the anulus fibrosus exhibits a distinct layered pattern reflective of its' lamellar structure, whereas the nucleus region is relatively homogeneous.

To experimentally demonstrate the utility of the first-order algorithm, MR data from a true deformation experiment (i.e., images of an unloaded and loaded specimen) was collected. A cylindrical tissue phantom (8.6-mm diameter $\times$ 25-mm length) was created by suspending cotton fibers within an agarose hydrogel (1.5% by weight, Bio-Rad Laboratories). A contrast agent (Magnevist, Berlex Imaging) was included in the hydrogel mixture at a concentration of 0.5% by volume to shorten the T1 relaxation time. The specimen was placed in a modified syringe tube having the same inner radius as the hydrogel and containing a fixed platen at the bottom. A compressive load could be applied to the specimen by inserting a modified syringe plunger in the tube. Fluid was allowed to escape the tube via four 1-mm-diameter drainage holes spaced along the height of the tube. This loading system roughly approximates a uniaxial confined compression test configuration [21], except that the fluid exudation occurs radially (and nonuniformly) through the holes rather than uniformly in the loading direction through a porous loading platen.

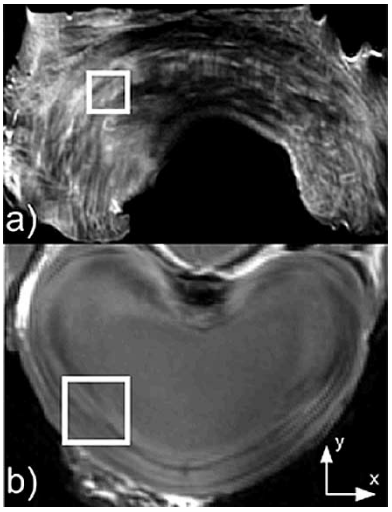

Fig. 1. Representative 2-D axial MR images of (a) canine meniscus and (b) porcine intervertebral disc. Superimposed squares identify representative 21×21 pixel subset masks.

A tare load was first applied to the specimen to assure full contact with the plunger, and the loading device was sealed and placed in a 9.4-T scanner to acquire a 3-D "unloaded" data set (standard spin-echo sequence, $256 \times 256 \times 64$ matrix size, 78 $\mu\mathrm{m}^3$ voxel size, $\mathrm{TR} = 1$ (reference), 1.5 s (loaded), $\mathrm{TE} = 12$ ms,). The device was removed and loaded by compressing the plunger 1.9 mm, corresponding to a nominal (axial) strain value of 7.5%. The device was replaced in the scanner and MRI acquisition was repeated to obtain the "loaded" data set.

B. First-Order Versus Zeroth-Order Texture Correlation

For the meniscus and intervertebral disc images described above, tissue deformation was simulated by applying to the reference image a quadratically varying, one-dimensional displacement field combined with a nonuniform, linearly varying rotational displacement field ($\Delta\theta = 0.05\theta$) given by

$$\begin{aligned} U(x,y) &= r\cos(\Delta\theta) \\ V(x,y) &= r\sin(\Delta\theta) + a_1 y^2 \end{aligned} \tag{5}$$

where U and V are the resulting x and y displacements, respectively, a_1 is a constant, and r is the radial distance for a given pixel from the upper right-hand corner of the image. Bicubic spline interpolation was used to determine intermediate pixel values for the deformed image. This displacement field resulted in strain distributions with $\mathrm{E_{yy}}$ (the y-component of Lagrangian strain) varying from 6%–10% and $\mathrm{E_{xx}}$ varying from 0%–1% for the areas of the images examined. Zeroth-order and first-order texture correlation algorithms were used to track a grid of points ($\mathrm{n} = 80$ for the meniscus, $\mathrm{n} = 60$ for the disc) on each test image. A subset mask size of 21×21 pixels was used for both algorithms, and discrete interpolation for the zeroth-order algorithm was carried out to the nearest 1/16th pixel. The displacement data

were input as nodal displacements of a mesh of 2-D quadratic plane-strain elements using standard finite element software (ANSYS 7.0, Canonsburg, PA) to obtain the components of 2-D strain. Average displacement error and the resulting nodal strain error ($n = 128$ for meniscus, $n = 172$ for disc) were then calculated for the two algorithms and compared using a Student's t-test, with $p < 0.05$ considered to be statistically significant.

C. Dependence of Texture Correlation on Image Noise

To assess the effects of image noise on displacement tracking accuracy, unique sets of Gaussian-distributed noise were independently superimposed on the complex deformation image pairs described above. Correlation was performed with both zeroth-order and first-order algorithms for a range of superimposed noise levels, and the average strain error across all points and for each noise level [signal-to-noise ratio (SNR)] were calculated.

The effect of noise filtering on texture correlation accuracy was examined using the same complex deformation image pairs with superimposed noise described earlier. Noise filtering was carried out by applying an adaptive Wiener filter (which minimizes the least squares error between the reconstructed and noiseless images) [22] to the image pair prior to performing correlation with the first-order texture correlation algorithm. The average strain error was calculated at various levels of SNR and compared with the unfiltered case using a paired t-test.

D. Dependence of Tracking Error on Image Texture

Distinct patterns (texture) within an image are necessary to accurately track pixel displacement with texture correlation. Thus, displacement error in relatively heterogeneous regions of an image (e.g., anulus fibrosus of the disc) should be less than in the more homogeneous nucleus pulposus. To illustrate this, we compared the average radial error for pixels located in the anulus fibrosus of a typical disc image to pixels located within the nucleus region of the same image for various levels of SNR. For this analysis, a linear displacement gradient equivalent to a 6% uniform strain was used to create a loaded image so that the effects of image texture on measurement error could be completely isolated.

In order to estimate whether a given tissue and MR image conditions are adequate for texture correlation measurement, a predictor of accuracy is desirable. This estimate of tracking error would allow the texture correlation user to adaptively select a grid of pixels for tracking (e.g., refining a grid of tracking points in an area of low expected error to obtain highly accurate strain fields). For a pixel to be accurately tracked, the features (intensity variations) within the pixel's subset mask should be significantly larger than the background noise. Based on this reasoning, we chose to examine the ratio of the standard deviation of intensity for a pixel's subset mask divided by the standard deviation of background, which we termed the roughness index, β. The roughness index β was calculated for each pixel within representative meniscus and disc images with superimposed noise (SNR = 20) in order to understand how texture is distributed spatially within a typical MR image. To determine if β is an appropriate measure of error, average radial error was plotted versus β for each tracking point of the uniform strain image pairs at various levels of SNR.

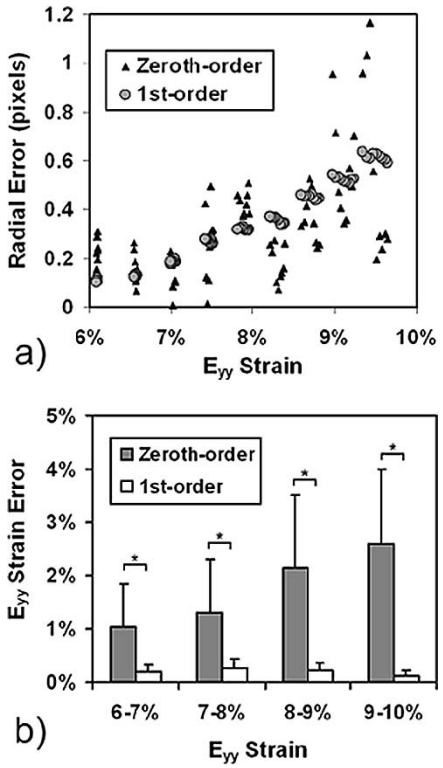

Fig. 2. a) Displacement tracking error (radial error) versus simulated strain level for zeroth-order and first-order texture correlation algorithms in a representative meniscus image (80 tracking points for each algorithm) with simulated complex deformation field. The zeroth-order algorithm exhibits much more random error, particularly at higher levels of strain. b) Average nodal strain error as a function of applied strain for meniscus images for zeroth- and first-order algorithms ($n = 64$ for 6%-7% and 7%-8%, $n = 80$ for 8%-9%, and $n = 48$ for 9%-10%), * indicates $p < 0.05$.

E. Experimental Strain Field Determination

Although the computer simulations described above are valuable in comparing algorithm performance, they cannot acceptably duplicate confounding factors such as intra-pixel volume averaging or additive random image noise that are encountered in actual experimental imaging. To test the performance of the first-order algorithm in actual experimental conditions, a 2-D axial (parallel to loading direction) image pair was extracted from the unloaded and loaded 3-D tissue phantom data sets, and a 5×6 grid of tracking points (30 points, each point spaced 5 pixels apart) were tracked between the pair using the first-order texture correlation algorithm (subset mask size: 21×21 pixels). Texture correlation-generated displacement data (U_0 and V_0) for each pixel were input as nodal displacements using standard finite element software as described above to obtain the 2-D strain components. For comparison, a second image pair from a parallel plane located 12 pixels (0.94 mm) away was extracted from the data sets and analyzed in the same manner.

IV. Results

A. First-Order Texture Correlation With MR Images

For the meniscus images examined, there was no significant difference in average radial error for the first-order algorithm as compared with the zeroth-order algorithm (0.33 ± 0.17 versus 0.31 ± 0.20 pixels, respectively). Fig. 2(a) shows average displacement error as a function of increasing strain level within

a given meniscus image for both algorithms. It was noted that the first-order algorithm exhibits a conspicuous displacement bias error which increases for increasing levels of simulated strain, while the zeroth-order algorithm exhibits a comparable but much more random error. When these displacement fields are differentiated to obtain strain, the displacement bias error of the first-order algorithm translates to significantly less strain error than the zeroth-order algorithm, as shown in Fig. 2(b) for one component of strain (E_{yy}). The zeroth-order algorithm exhibited increasing strain error (up to 2.6%) with increasing levels of strain, while the first-order algorithm strain error did not (with values that never exceeding 0.25%). Differences in strain error between the two algorithims were statistically significant at all levels of superimposed strain. For a subset mask size of 21×21 pixels, the first-order algorithm had an average computation time (per tracking point) of 3.1 s, as compared to 1.2 s for the zeroth-order algorithm. Simulations were performed on a 1.5-GHz Pentium M computer with 512 MB RAM.

Average strain errors for the disc images were also significantly lower using the first-order algorithm (e.g., average error in $E_{yy} = 0.39\% \pm 0.27\%$) as compared to the zeroth-order algorithm ($2.34\% \pm 2.19\%$, $p < 0.001$). As with the meniscus images, more random displacement error was noted with the zeroth-order algorithm.

B. Dependence of Texture Correlation on Image Noise

The effects of image noise on average strain error for meniscus images are shown in Fig. 3. Again, no significant difference in displacement error was noted between the two algorithms for any of the noise levels investigated (data not shown), but strain error was significantly lower when using the first-order algorithm for noise levels of SNR $= 20$ and higher. For SNR $= 10$, both algorithms exhibited high amounts of strain error ($\geq 6\%$), with no significant differences between the two algorithms. Both algorithms exhibited decreasing displacement error and strain error with increasing SNR. For disc images, adding image noise led to such high errors in displacement measurement that strain fields could not be computed for SNR levels less than 40. The highest displacement errors were noted to occur in the homogeneous nucleus pulposus region of the image. However, at SNR $= 40$, the improved performance of the first-order algorithm was evident with measures of strain error in E_{yy} of $0.98\% \pm 1.16\%$ as compared to $3.36\% \pm 3.19\%$ for the zeroth-order algorithm ($p < 0.001$).

Applying the Wiener noise removal filter prior to texture correlation analysis reduced strain measurement error for all levels of SNR for the meniscus images, as shown in Fig. 4. Reductions in strain error ranged from 20%–56%, with the most dramatic improvements for the low SNR image pairs. However, for the disc images examined (SNR $= 40$ only), use of the filter led to no detectable reductions in strain error (data not shown).

C. Dependence of Tracking Error on Image Texture

The preceding results demonstrate that there are significant differences in image texture between meniscus and disc images. We found that at lower levels of SNR, the points located in the "feature-rich" anulus fibrosus exhibit less displacement error on average as compared to the more homogeneous nucleus pulposus (0.54 ± 0.72 pixels for anulus versus 5.59 ± 6.71 pixels,for nucleus, first-order algorithm, SNR $= 10$). This spatial difference in accuracy is reduced at higher levels of SNR (0.05 ± 0.02 pixels for anulus versus 0.13 ± 0.08 pixels for nucleus, SNR $= 60$) and is not distinguishable at SNR levels of approximately 60 or greater. For the meniscus images, there was no evidence of differences in error with variations in spatial position for any levels of SNR (data not shown).

Fig. 5 shows computed β values for each pixel within representative disc and meniscus MR images (superimposed noise

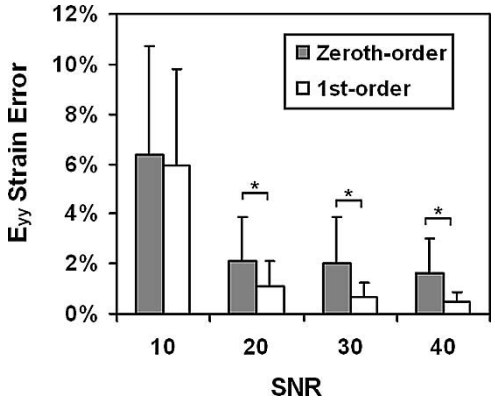

Fig. 3. Average strain error error versus SNR for meniscus images with complex deformation field analyzed with zeroth- and first-order texture correlation ($n = 256$ for each algorithm at each noise level). * indicates $p < 0.05$.

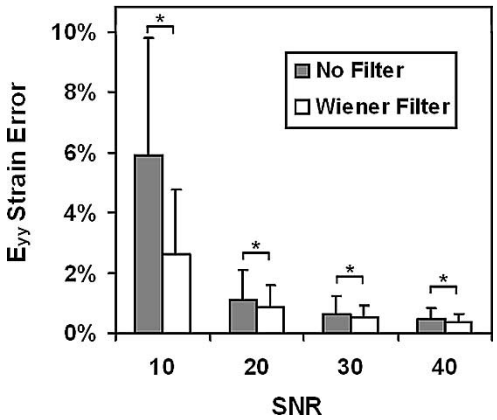

Fig. 4. Average strain error versus SNR for meniscus images with and without the application of adaptive (Wiener) noise removal filter ($n = 256$ per noise level for each case), * indicates $p < 0.05$.

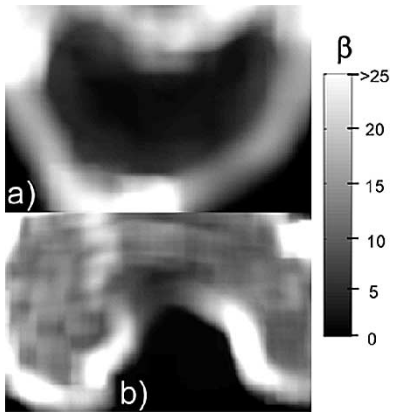

Fig. 5. Roughness index, β, mapped for each pixel within representative 2-D MR images with superimposed Gaussian distributed noise. (a) Intervertebral disc and (b) meniscus. Roughness index values calculated based on 21×21 pixel subsets for each pixel, SNR $= 40$ for both images.

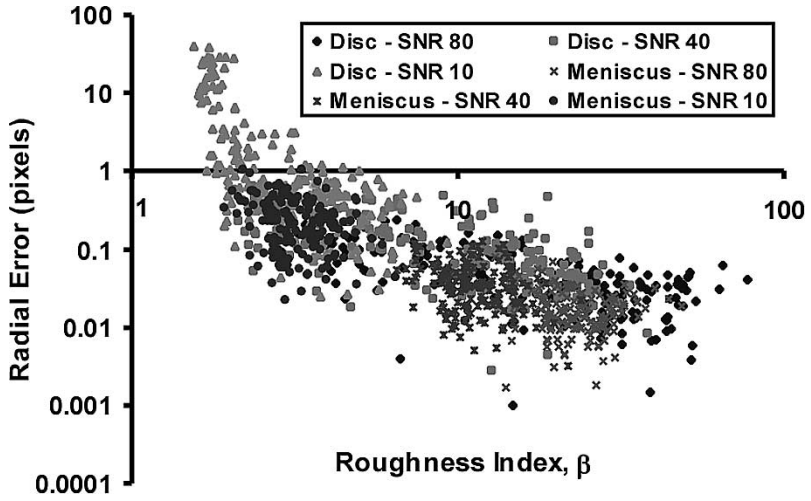

Fig. 6. Radial error as a function of roughness index, β, for 6% simulated biaxial strain. Roughness index values calculated based on 21 × 21 pixel subsets for each pixel.

levels of SNR $= 40$). Note that the homogeneous nucleus pulposus region can be identified by lower values of β, as compared with the anulus fibrosus region. Some of this difference can be attributed to the large change of intensity at the edge of the tissue: a typical point in the anulus fibrosus region (SNR $=$ 40) whose subset includes the tissue edge had a β of 16.6 ± 5.5 ($\mathrm{n} = 14$), a point located in the lamellar anulus fibrosus region but not including an edge had a β of 7.0 ± 2.0 ($\mathrm{n} = 14$), and a point located in the nucleus pulposus had a β of 2.6 ± 0.4 ($\mathrm{n} = 14$). The meniscus image (SNR $= 40$) exhibits higher overall levels of β than the disc, and shows less difference in β with spatial position in the tissue. Points located completely within the meniscus tissue had β values of 13.4 ± 1.6 ($\mathrm{n} = 20$), while points whose pixel subset contain a tissue edge had average β values of 24.4 ± 4.3 ($\mathrm{n} = 20$).

Next, the roughness index β for each tracking point within each image ($\mathrm{n} = 63$ for each disc image, $\mathrm{n} = 80$ for each meniscus image) was plotted versus radial error for superimposed noise levels of SNR $= 10$, 40, 80, as shown in Fig. 6. The plot shows a decreasing level of displacement error with increasing roughness index, independent of SNR. This result suggests that β is an appropriate parameter for estimating texture correlation displacement measurement error (and, hence, strain error) from MR images for any tissue type or noise level.

D. Experimental Strain Field Determination

An axial image slice (Slice 1) extracted from the "unloaded" 3-D data set is shown in Fig. 7(a), with the direction of loading and locations of the pixels where displacement was tracked identified. Average SNR for the 2-D slices was calculated to be 40.4. The mean roughness index β of the 30 points tracked was 5.4 ± 1.0 for Slice 1 and 6.0 ± 1.4 for Slice 2. Axial strain ($\mathrm{E_{yy}}$) maps for Slice 1 and Slice 2 (a parallel plane 0.94 mm away) generated from the texture correlation results are shown in Fig. 7(b). Both slices exhibit a similar strain pattern in the loading direction, with a region of high compressive strain near the top of the mapped area and lower values of strain in the remaining mapped area. The top row of elements was found to have an average strain of $-9.55\% \pm 2.59\%$ for Slice 1 and $-9.07\% \pm 2.71\%$ for Slice 2 (negative values indicate compressive strain). Local values of axial strain varied from -20% to $+2\%$. Radial strains ($\mathrm{E_{xx}}$) were found to be much smaller and more uniform within the examined area, with average strains of $0.17\% \pm 0.83\%$ and $-0.14\% \pm 0.52\%$ for Slices 1 and 2, respectively.

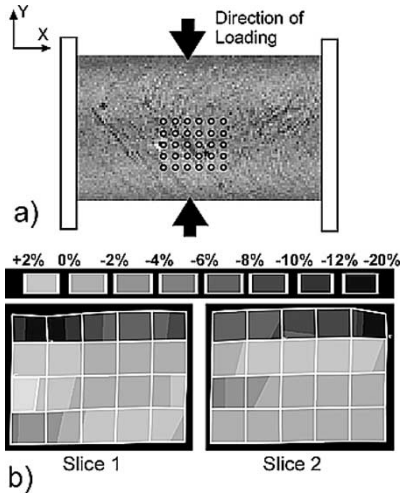

Fig. 7. Experimental strain determination in hydrogel tissue phantom using first-order texture correlation: a) Test configuration schematic showing 2-D axial MR image slice (Slice 1) and pixel grid used for displacement tracking. b) pixel grid in deformed configuration with contours of 2-D axial ($\mathrm{E_{yy}}$) strain for two axial slices located 12 pixels (0.94 mm) apart, generated from texture correlation displacement data ($\mathrm{U_0}, \mathrm{V_0}$). Positive strain values indicate tension, negative indicate compression.

V. Discussion

The results shown in Figs. 2 and 3 indicate that a first-order texture correlation algorithm can significantly improve strain measurement accuracy in MR images, as compared with a zeroth-order algorithm. The first-order algorithm showed significantly improved performance in MR images, and showed no dependence of strain error on the level of simulated strain. Conversely, the zeroth-order algorithm exhibited much more random displacement errors that led to much higher errors in strain field measurement.

Since the first-order algorithm essentially involves differentiation of the image intensity, it was anticipated that use of this algorithm to calculate strain fields would be complicated by the noise associated with high-resolution MR images. While strain error was indeed found to correlate with SNR for the meniscus images, noise did not prevent accurate determination of strain fields as compared with the zeroth-order algorithm, for SNR levels of 20 and greater. Additionally, use of an adaptive Wiener noise removal filter prior to texture correlation analysis was effective in reducing measurement error for meniscus images, particularly for high levels of noise. For the disc images examined, the first-order algorithm showed significant reduction in displacement and strain error compared with the zeroth-order algorithm. However, with the added effects of image noise the homogeneous nucleus pulposus region did not provide adequate texture for accurate strain measurements with either algorithm at SNR levels less than 40.

In previous studies of DIC with optical imaging, quantification of texture has not been an issue since image heterogeneity can be controlled (e.g., adding laser speckle) and image noise is typically low [23]. MRI texture correlation offers the advantage of determining displacement measurement without artificial markers or speckle, allowing biomechanical study of intact tissues and joints. However, MR image texture is directly dependent on the intrinsic structure and composition of the tissue being imaged. The findings presented here demonstrate that differences in tissue imaging properties between tissues and at various locations within a given tissue can result in significant differences in displacement measurement accuracy using MRI texture correlation. Disc images exhibited much larger average radial errors than meniscus images at similar levels of noise, largely due to tracking points located within the homogeneous nucleus pulposus regions of the disc.

We have shown that a quantitative measure of texture, defined as the roughness index, β, correlates well with accuracy in displacement tracking across a broad spectrum of MR image regions. The higher standard deviations in β and radial error in the anulus fibrosus region as compared with the meniscus suggest that the amount of texture is different (less consistent in the anulus fibrosus) between these two tissues types. For the current study no attempt to find an explicit relationship between β and displacement error was made. However, from the preceding observations and the demonstrated correlation between β and average radial error, it is apparent that the roughness index for a given MR image can help the user decide if a given type of tissue, location within a tissue, or image noise level are adequate to provide acceptable accuracy in displacement tracking and strain measurement. Specifically, it may be possible to use β values to determine what tracking point grid spacings (and resulting finite element meshes) are appropriate for various locations within a tissue, based on expected tracking error. This would potentially result in more accurate strain field determination.

The results of our initial strain estimates for a tissue-mimicking hydrogel yielded reasonable results and indicate the potential for MR texture correlation to detect high-resolution heterogeneous strain patterns within tissues. For an isotropic hydrated material in ideal confined compression [21], axial strains would be predicted to be uniform and equal to the nominal strain value (7.5% for this case). Our strain analyzes estimated compressive strains that encompassed this magnitude, but were highly heterogeneous in nature. This heterogeneity in axial strain estimates may reflect friction between the sample and loading apparatus, inhomogeneity in the sample, nonuniform fluid flow, or other discrepancies in our nonideal testing configuration. Radial strains were measured to be highly uniform, however, and more than one order of magnitude less than axial strains, in reasonable agreement with predictions of zero radial strains for this configuration. Additional experiments using a calibration phantom will prove useful for illustrating the accuracy of the first-order texture correlation algorithm for determining strain fields under actual experimental conditions with MR images.

One limitation in the current investigation was the study of only two simulated displacement fields (linear and higher-order gradients), with strain levels varying from 6%–10%. It is expected that differences between first-order and zeroth-order algorithms will be reduced for lower levels of deformation, since strain error for the zeroth-order algorithm was shown to correlate with strain level. Additionally, a potential dependence of sample orientation was not investigated in this study. It is known that the T2 relaxation time of collagenous tissues depends on the orientation of collagen fibers within the magnetic field. For tissues such as the meniscus, which features radially distributed collagen fibers, it may be necessary to combine image information taken at several orientations to produce maximum texture for the entire tissue. Finally, in actual experiments based on consecutive reference and loaded MR images, additional error will be introduced due to out-of-plane tissue displacements, variations in imaging conditions, and potentially due to change in imaging properties of the tissue as fluid is released under load. Thus, care should be used when extrapolating the findings from the simulated data to actual experimental conditions. However, the reduced strain error observed with the first-order displacement mapping algorithm, as well as the observed relationships between error and imaging parameters (e.g., SNR), will pertain to actual experimental conditions. In particular, implementation of the roughness index to reduce measurement error, as proposed here, can be expected to impact algorithm performance for actual experiments. While only two tissue types were examined in this study, they contain a variety of texture and structural heterogeneities that suggest the broader utility of the proposed method. Improvement of the results presented here should be possible by introducing optimized displacement smoothing [24] to displacement field results prior to strain computation. Also, extending the first-order technique to three dimensions will be important to fully account for the out-of-plane deformations that occur in many tissues.

VI. Conclusion

The results of this study indicate that first-order texture correlation is useful for improving accuracy in strain field measurement with MR images, particularly for tissues undergoing larger deformations. Additionally, this study represents a first attempt to quantify texture within MR images and understand how it relates to error in displacement tracking using a first-order texture

correlation algorithm. By quantifying the amount of texture for a given tissue MR image with the newly defined roughness index, the texture correlation user can better estimate *a priori* whether test conditions and tissue type will yield acceptable measurement accuracy. This may prove to be a valuable tool toward the goal of determining high-resolution 2-D and 3-D deformation and strain fields within biologic materials using MR texture correlation.

REFERENCES

[1] F. Guilak, R. L. Sah, and L. A. Setton, "Physical regulation of cartilage metabolism," in *Basic Orthopaedic Biomechanics*, V.C. Mow and W.C. Hayes, Eds. Philadelphia, PA: Lippincott-Raven, 1997, pp. 179–207.

[2] J. P. G. Urban *et al.*, "The effect of physical factors on disc cell metabolism," in *Musculoskeletal Soft-Tissue Aging: Impact on Mobility*, J.A. Buckwalter *et al.*, Eds. Rosemont, IL: Amer. Acad. Orthop. Surg., 1993, pp. 391–412.

[3] A. J. Banes, M. Tsuzaki, J. Yamamoto, T. Fischer, B. Brigman, T. Brown, and L. Miller, "Mechanoreception at the cellular level: The detection, interpretation, and diversity of responses to mechanical signals," *Biochem. Cell Biol.*, vol. 73, pp. 349–365, 1995.

[4] M. A. LeRoux, J. Arokoski, T. P. Vail, F. Guilak, M. M. Hyttinen, I. Kiviranta, and L. A. Setton, "Simultaneous changes in the mechanical properties, quantitative collagen organization, and proteoglycan concentration of articular cartilage following canine meniscectomy," *J. Orthop. Res.*, vol. 18, no. 3, pp. 383–392, 2000.

[5] A. Kerin, P. Patwari, K. Kuettner, A. Cole, and A. Grodzinsky, "Molecular basis of osteoarthritis: Biomechanical aspects," *Cellular Molecular Life Sci.*, vol. 59, pp. 27–35, 2002.

[6] C. B. Frank, D. A. Hart, and N. G. Shrive, "Molecular biology and biomechanics of normal and healing ligaments—A review," *Osteoarthritis Cartilage*, vol. 7, pp. 130–140, 1999.

[7] D. B. Plewes, J. Bishop, A. Samani, and J. Sciarretta, "Visualization and quantification of breast cancer biomechanical properties with magnetic resonance elastography," *Phys. Med. Biol.*, vol. 45, no. 6, pp. 1591–1610, 2000.

[8] E. A. Zerhouni, D. M. Parish, W. J. Rogers, A. Yang, and E. P. Shapiro, "Human heart: Tagging with MR imaging—A method for noninvasive assessment of myocardial motion," *Radiology*, vol. 169, no. 1, pp. 59–63, 1988.

[9] K. L. Wedding, M. T. Draney, R. J. Herfkens, C. K. Zarins, C. A. Taylor, and N. J. Pelc, "Measurement of vessel wall strain using cine phase contrast MRI," *J. Magn. Reson. Imag.*, vol. 15, pp. 418–428, 2002.

[10] A. H. Aletras, S. Ding, R. S. Balaban, and H. Wen, "DENSE: Displacement encoding with stimulated echoes in cardiac functional MRI," *J. Magn. Reson.*, vol. 137, pp. 247–252, 1999.

[11] C. Herberhold, T. Stammberger, S. Faber, R. Putz, K. H. Englmeier, M. Reiser, and F. Eckstein, "An MR-based technique for quantifying the deformation of articular cartilage during mechanical loading in an intact cadaver joint," *Magn. Reson. Med.*, vol. 39, no. 5, pp. 843–850, 1998.

[12] A. E. Bowden, R. D. Rabbitt, and J. A. Weiss, "Anatomical registration and segmentation by warping template finite element models," in *Proc. SPIE Biomedical Optics Symp.*, vol. 3254, pp. 469–476.

[13] A. I. Veress, J. A. Weiss, G. T. Gullberg, D. G. Vince, and R. D. Rabbitt, "Strain measurement in coronary arteries using intravascular ultrasound and deformable images," *J. Biomech. Eng.*, vol. 124, pp. 734–741, 2002.

[14] M. A. Sutton, S. R. McNeill, J. D. Helm, and Y. J. Chao, "Advances in two-dimensional and three-dimensional computer vision," in *Topics in Applied Physics: Photomechanics*, P.K. Rastogi, Ed. Berlin, Germany: Springer-Verlag, 1999, vol. 77, pp. 323–368.

[15] G. Vendroux and W. G. Knauss, "Submicron deformation field measurements: Part 2. Improved digital image correlation," *Exp. Mech.*, vol. 38, no. 2, pp. 86–92, 1998.

[16] B. K. Bay, "Texture correlation: A method for the measurement of detailed strain distributions within trabecular bone," *J. Orthop. Res.*, vol. 13, no. 2, pp. 258–267, 1995.

[17] D. P. Nicolella, A. E. Nicholls, J. Lankford, and D. T. Davy, "Machine vision photogrammetry: A technique for measurement of microstructural strain in cortical bone," *J. Biomech.*, vol. 34, no. 1, pp. 135–139, 2001.

[18] M. J. Bey, H. K. Song, F. W. Wehrli, and L. J. Soslowsky, "A noncontact, nondestructive method of quantifying intratissue deformations and strains," *J. Biomech. Eng.*, vol. 124, no. 2, pp. 253–258, 2002.

[19] T. C. Chu, W. F. Ranson, M. A. Sutton, and W. H. Peters, "Applications of digital-image-correlation techniques to experimental mechanics," *Exp. Mech.*, vol. 25, no. 3, pp. 232–244, 1985.

[20] H. Lu and P. D. Cary, "Deformation measurements by digital image correlation: Implementation of a second-order displacement gradient," *Exp. Mech.*, vol. 40, no. 4, pp. 393–400, 2000.

[21] M. H. Holmes, "Finite deformation of soft tissue: Analysis of a mixture model in uni-axial compression," *J. Biomech. Eng.*, vol. 108, pp. 372–381, 1986.

[22] R. C. Gonzalez and P. Wintz, *Digital Image Processing*. Reading, MA: Addison-Wesley, 1988.

[23] M. A. Sutton, S. R. McNeill, J. Jang, and M. Babai, "Effects of subpixel image restoration on digital correlation error estimates," *Opt. Eng.*, vol. 27, no. 10, pp. 870–877, 1988.

[24] C. C. B. Wang, J. M. Deng, G. A. Ateshian, and C. T. Hung, "An automated measurement of two-dimensional strain distributions within articular cartilage under unconfined compression," *J. Biomech. Eng.*, vol. 124, pp. 557–566, 2002.